Single-molecule and -particle probing crystal edge/corner as highly efficient photocatalytic sites on a single TiO$_2$ particle

Wei-Kang Wang[a,b,c,1], Jie-Jie Chen[a,1], Zai-Zhu Lou[b,1], Sooyeon Kim[b], Mamoru Fujitsuka[b,2], Han-Qing Yu[a,2], and Tetsuro Majima[b,2]

[a]Chinese Academy of Sciences Key Laboratory of Urban Pollutant Conversion, Department of Applied Chemistry, University of Science & Technology of China, 230026 Hefei, China; [b]The Institute of Scientific and Industrial Research, Osaka University, Ibaraki, 567-0047 Osaka, Japan; and [c]Department of Chemistry, Tongji University, 200000 Shanghai, China

The exposed active sites of semiconductor catalysts are essential to the photocatalytic energy conversion efficiency. However, it is difficult to directly observe such active sites and understand the photogenerated electron/hole pairs' dynamics on a single catalyst particle. Here, we applied a quasi-total internal reflection fluorescence microscopy and laser-scanning confocal microscopy to identify the photocatalytic active sites at a single-molecule level and visualized the photogenerated hole–electron pair dynamics on a single TiO$_2$ particle, the most widely used photocatalyst. The experimental results and density functional theory calculations reveal that holes and electrons tend to reach and react at the same surface sites, i.e., crystal edge/corner, within a single anatase TiO$_2$ particle owing to the highly exposed (001) and (101) facets. The observation provides solid proof for the existence of the surface junction "edge or corner" on single TiO$_2$ particles. These findings also offer insights into the nature of the photocatalytic active sites and imply an activity-based strategy for rationally engineering catalysts for improved photocatalysis, which can be also applied for other catalytic materials.

photocatalyst | TiO$_2$ | single-molecule microscopy | single-particle microscopy | crystal edge/corner

Photocatalysis is an efficient and sustainable way to harness the inexhaustibly abundant, clean, and safe energy of the Sun (1, 2). Titanium oxide (TiO$_2$) with different crystal structures and various morphologies has great potential as an ideal and powerful photocatalyst for various reactions owing to its chemical stability, nontoxicity, and high reactivity (3, 4). The efficient separation and transfer of photogenerated electron–hole pairs are well known to play an important role in photocatalysis. First, photoexcitation of TiO$_2$ generates hole–electron pairs of which electrons are trapped at the defects (for example, oxygen vacancies) and/or donor impurities (5–7). The behavior of the trapped electrons has a great impact on the properties of TiO$_2$, including the optical absorption, the electrical conductivity, and the chemical reactivity (8, 9). Second, the photogenerated electrons can transfer from (001) to (101) facets owing to their relative levels of conduction band minimum (10–15). The electron transport property of anatase TiO$_2$ is essential in photocatalysis, where the electron trapping sites can severely limit the overall performance (16, 17). Understanding the behavior of electrons in anatase TiO$_2$ is thus crucial for improving the photocatalytic performance of TiO$_2$.

Photocatalytic reactions and their mechanisms in TiO$_2$ have been explored using a number of spectroscopies (18–27). Scanning tunneling microscopy was used to in situ explore the molecular oxygen adsorption behaviors (28), adsorption sites for CO (29), photocatalytic dissociation of water (30), and roles of point defect in TiO$_2$ surface (31). Recently, photogenerated charge carriers on surfaces and interfaces of photocatalysts could be directly measured by using spatially resolved surface photovoltage microscopy (SPV) (32–36). Furthermore, in particular, kelvin probe force microscopy (KPFM) (37) based on spatially resolved SPV techniques

could be applied in charge separation imaging (38–40). Meanwhile, a current-mapping image of the photoelectrodes was measured by photoconductive atomic force microscope (41–44).

Moreover, a spatial correlation between hole- and electron-induced redox reactions on TiO$_2$ nanorods with a cocatalyst was obtained by superresolution hole and electron reaction mapping (20, 45–47). Recently, the single-particle confocal fluorescence microscopic measurement was used as a direct tool to investigate the generation, transfer, separation, and recombination of electrons/holes on photocatalysts (48, 49). Charge carrier mobility and recombination can be investigated with spatially and temporally resolved photoluminescence (PL) measurements on individual anatase TiO$_2$ particles. Furthermore, the single-particle and -molecule images of TiO$_2$ photocatalytic reactions using total internal reflection fluorescence (TIRF) microscopy confirm the crystal-face–dependent photocatalytic reductive sites on individual anatase TiO$_2$ particles (18). Thus, single-particle detection can be used for direct visualization of the structure–activity relationship on TiO$_2$ particles, while single-molecule detection can be applied for a spatial correlation of redox reactions (50, 51).

In this work, the distribution of active sites on anatase TiO$_2$ particles was probed by using single-particle confocal fluorescence and TIRF microscopes. Also, the most active sites for charge-carrier

Significance

The exposed active sites of semiconductor catalysts are essential to the photocatalytic energy conversion efficiency. Here, we applied a quasi-total internal reflectance fluorescence microscopy and laser-scanning confocal microscopy to identify the photocatalytic active sites at a single-molecule level and visualized the photogenerated hole–electron pair dynamics on single TiO$_2$ particle. The experimental results and density functional theory calculations reveal that holes and electrons tend to reach and react at the same surface sites, i.e., crystal edge/corner, owing to the exposed (001) and (101) facets of TiO$_2$. These findings offer insights into the nature of photocatalytic active sites and imply an activity-based strategy for rationally engineering catalysts for improved photocatalysis, which could be also applied for other catalytic materials.

recombination in the single-particle spatiotemporal resolution were explored. Moreover, density functional theory (DFT) calculations were performed to connect the photocatalytic performance of the fluorogenic probe reactions on the surfaces and at the crystal edge with the location of the reaction sites. In this way, direct evidence can be obtained to identify crystal edge/corners as highly efficient catalytic sites for TiO_2 particles.

Results and Discussion

Characterization of the Obtained Sample. The TiO_2 nanoparticles are synthesized via the hydrothermal reaction. The power X-ray diffraction (XRD) patterns of the obtained samples in *SI Appendix,* Fig. S1*A* are in agreement with the standard anatase (JCPDS no. 21-1272), indicating that the samples were anatase TiO_2 and the peaks from other phases were not overlapped. As shown in *SI Appendix,* Fig. S1*B*, the anatase TiO_2 particles are uniform with an average size of 2 to 3 μm. In the high-magnification micrograph (*SI Appendix,* Fig. S1*B*, *Inset*) and TEM image (*SI Appendix,* Fig. S1*C*), the surface of the anatase TiO_2 particle was smooth (or flat) without small particles. The distinguished 1D lattice fringes in *SI Appendix,* Fig. S1*D* indicate that the obtained TiO_2 was well crystallized with a lattice fringe spacing of 0.19 nm (measured by digital micrograph), corresponding to the (001) facet of anatase TiO_2. The selected-area electron diffraction (SAED) (*SI Appendix,* Fig. S1*D*, *Inset*) confirms the formation of anatase TiO_2 particles with a highly exposed (001) facet. Moreover, the XPS analysis was performed to explore the adsorbed fluorine ions on TiO_2 particles (*SI Appendix,* Fig. S2). Thus, the removal of adsorbed fluorine ions on TiO_2 particles was confirmed as no peak of F 1s was observed (*SI Appendix,* Fig. S2*C*). The C 1s peak observed in the survey came from the background (*SI Appendix,* Fig. S2*D*).

Single-Particle PL Images on a Single TiO_2 Particle. It is essential to clarify the mechanisms for the high-photocatalytic activities especially near the edges and corners of anatase TiO_2 particles. Single-particle spectroscopic measurements were performed to explore the electron transfer and PL lifetime in a single anatase TiO_2 particle as shown in Fig. 1*A*. Fig. 1*C* shows a typical single-particle PL lifetime mapping of a single anatase TiO_2 particle, while *SI Appendix,* Fig. S3*A* illustrates a phase-contrast microscopic image of the corresponding TiO_2 particle (red arrow). In addition, the single TiO_2 particle on a grid cover glass was confirmed with respect to its SEM image in Fig. 1*B* and *SI Appendix,* Fig. S3*B*.

Thus, the single-particle PL lifetime image can be investigated with the dependence on spatially resolved surfaces. First, it indicates that the PL lifetime on the middle of a single anatase TiO_2 particle was relatively shorter (Fig. 2*A*). Meanwhile, the longest PL lifetime was observed at the around-surface heterojunction of (001) and (101) facets, suggesting that the charge lifetimes were longer at the around-surface heterojunction than those in the middle of the surface. Fig. 2*B* and *SI Appendix,* Fig. S4 illustrate several sites of a single anatase TiO_2 particle. The normalized PL spectra at several sites on a single anatase TiO_2 particle were measured as shown in Fig. 2*C*. The PL peak at 630 nm originates from the charge recombination on the surface of a single anatase TiO_2 particle (52). The normalized PL intensity increased along the line from the middle area (site S_m) to the edge (sites E_{101}) and the corners (site C). The single-particle PL spectra at several sites exhibited no obvious spectral shift. Moreover, the PL intensities observed at the certain facet with the same spatial characters (surface S_1 to S_4, edge $E_{001\text{-}1}$ to $E_{001\text{-}4}$, and edge $E_{101\text{-}1}$ to $E_{101\text{-}4}$, and corner C_1 to C_4) are almost the same (*SI Appendix,* Fig. S5). These results indicate that the varied photocatalytic activities of a single anatase TiO_2 particle depend on the crystal nature such as surfaces, edges, and corners.

Furthermore, to investigate the interfacial charge transfer in anatase TiO_2 particles, the PL decay profiles of anatase TiO_2 particles were measured. Fig. 2*D* shows the spatial variations in charge-carrier lifetimes within a single anatase TiO_2 particle. From site S_m to E_{101} and C, the intensity-weighted lifetime also increased, in agreement with the PL lifetime image results. Moreover, both sites E_{001} and E_{101} had a similar value of intensity-weighted
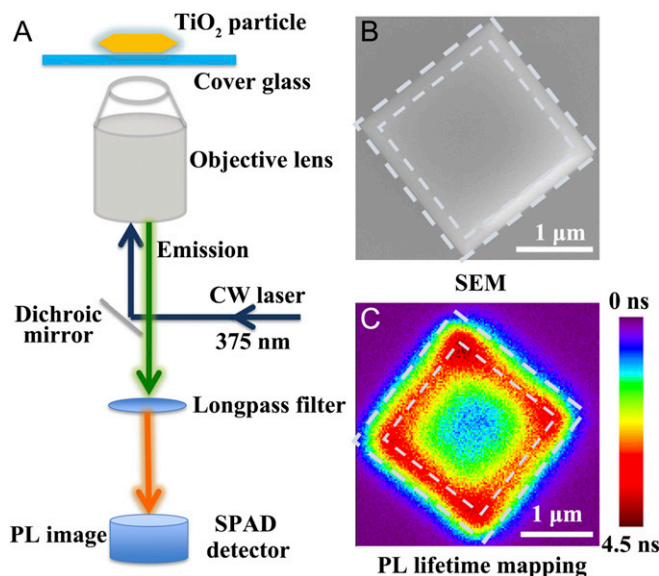

Fig. 1. (*A*–*C*) Experiment setup for single-particle PL measurements of a single anatase TiO_2 particle (*A*), the high-resolution SEM image of a single anatase TiO_2 particle (*B*), and the PL lifetime mapping of a single anatase TiO_2 particle with the colors standing for different lifetimes from single-particle PL measurements (*C*).

lifetime, indicating that the area near crystal edges is highly active sites (Fig. 2*D*). It was because that surface heterojunction exists in the area to promote the separation of the photogenerated charges. All sites such as surface S_1 to S_4, edge $E_{001\text{-}1}$ to $E_{001\text{-}4}$, edge $E_{101\text{-}1}$ to $E_{101\text{-}4}$, and corner C_1 to C_4 have similar lifetimes (*SI Appendix,* Fig. S6). The lifetimes at several sites of anatase TiO_2 particles are shown in *SI Appendix,* Fig. S7 *A* and *B* and Table S1.

According to the location of active sites on anatase TiO_2 particles, the intensity-weighted average lifetimes for the middle, surface, edge (in), edge (out), and corner were 1.50, 1.86, 3.05, 3.45, and 4.15 ns, respectively (Fig. 2*E*). This result is in good agreement with the PL intensity of anatase TiO_2 particles.

Similar results were obtained for other anatase TiO_2 particles with irradiation at other excitation wavelengths (375 and 405 nm as shown in Fig. 3 and *SI Appendix,* Fig. S8, respectively, and the images shown in *SI Appendix,* Figs. S9 and S10, respectively). Meanwhile, the lifetimes at several sites of 2 anatase TiO_2 particles (Fig. 3 *A* and *D*) are shown in *SI Appendix,* Fig. S7 *C*–*F* and Tables S2 and S3. These results further confirm the validity of our hypothesis that main hole–electron pairs are formed and transfered near the surface heterojunction (edges and corners) of anatase TiO_2 particles and they can indeed diffuse through the inner bulk of the particles to reach the surface. Moreover, the corner exhibited better electron transfer than the edge area because the former had a smaller coordination number and greater localized electric field enhancement. The detailed explanations are provided in *SI Appendix,* Part S1. This result indicates that the more highly active sites are near the surface heterojunction (edges and corners) of anatase TiO_2 particles.

Single-Molecule Probing of Photocatalytic Sites on a Single TiO_2 Particle. The photocatalytic redox reactions of TiO_2 particles were investigated at the bulk and single-particle level using 2 fluorogenic probes, i.e., amplex red and resazurin. Photogenerated holes (or consequent oxidizing species, such as surface-adsorbed hydroxyl radicals, OH radicals) were probed by the oxidative *N*-deacetylation of amplex red to resorufin, and photogenerated electrons were probed by the reductive *N*-deoxygenation of resazurin to resorufin. The UV-vis absorption and fluorescence spectra of the progress of photocatalytic oxidation are shown in *SI Appendix,* Fig. S11 *B* and *C*. Since amplex red did not absorb visible light, an increase in the absorption band at 570 nm clearly
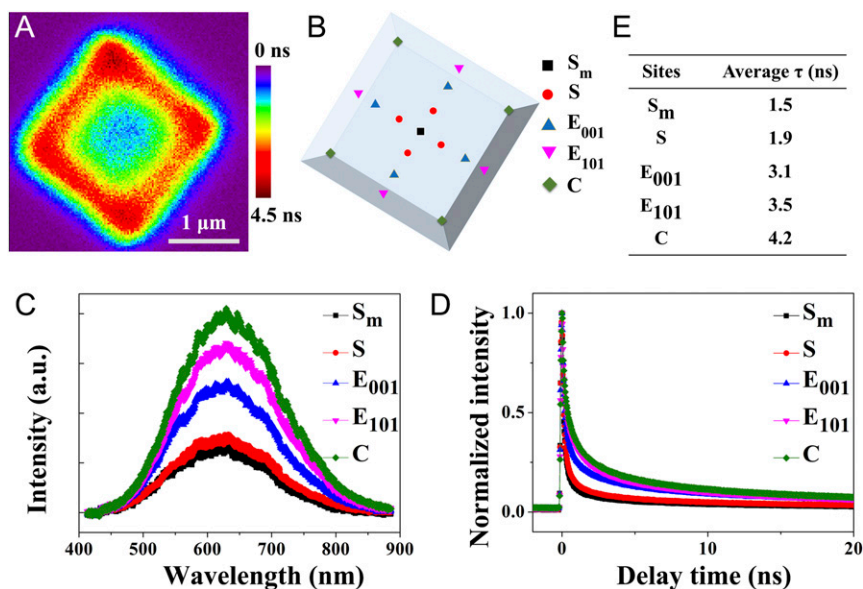
Fig. 2. (*A–E*) PL lifetime mapping of a single anatase TiO$_2$ particle and the color standing for different lifetimes (*A*), schematic sites of a single anatase TiO$_2$ particle (*B*), PL spectra (*C*), lifetime (*D*) observed at sites 1 to 4, and intensity-weighted lifetimes (*E*) on a single anatase TiO$_2$ particle.

demonstrates the formation of resorufin as a result of the photocatalytic oxidation of amplex red. Moreover, the peak of fluorescence at 570 nm increased simultaneously. The UV-vis absorption and fluorescence spectra of the progress of photocatalytic reduction are shown in *SI Appendix*, Fig. S11 *E and F*. The UV-visible absorption spectrum of resazurin in basic aqueous solutions consisted of an intense absorption band at 604 nm and a weak band at 380 nm, which are assigned to the $\pi\pi^*$ transition of the phenoxazin-3-one and to the weak $n\pi^*$ transition of the *N*-oxide, respectively (53). The absorption spectrum of resorufin was characterized by an intense band centered at 570 nm with a shoulder at 535 nm (53). Thus, according to the equation in *SI Appendix*, Fig. S11*D*, when

resazurin was reduced to resorufin, the weak $n\pi^*$ transition of the *N*-oxide of resazurin at 604 nm disappeared and a peak of resorufin was formed at 570 nm. Thus, the peak at 570 nm increased and the raw peak at 604 nm for resazurin decreased in the photocatalytic reduction of resazurin. Also, the peak of fluorescence at 570 nm for the highly fluorescent resorufin increased.

With the photocatalytic activity tests at the bulk level (*SI Appendix*, Fig. S11), fluorogenic reactions are validated to reflect the photocatalytic reactions of TiO$_2$ particles. Thus, it is feasible to apply fluorescence detection of resorufin to explore the interfacial electron transfer reactions on individual particles at the single-molecule level.

Furthermore, to view redox reactions and occurrence sites directly, a quasi-TIRF microscopy was used to investigate the
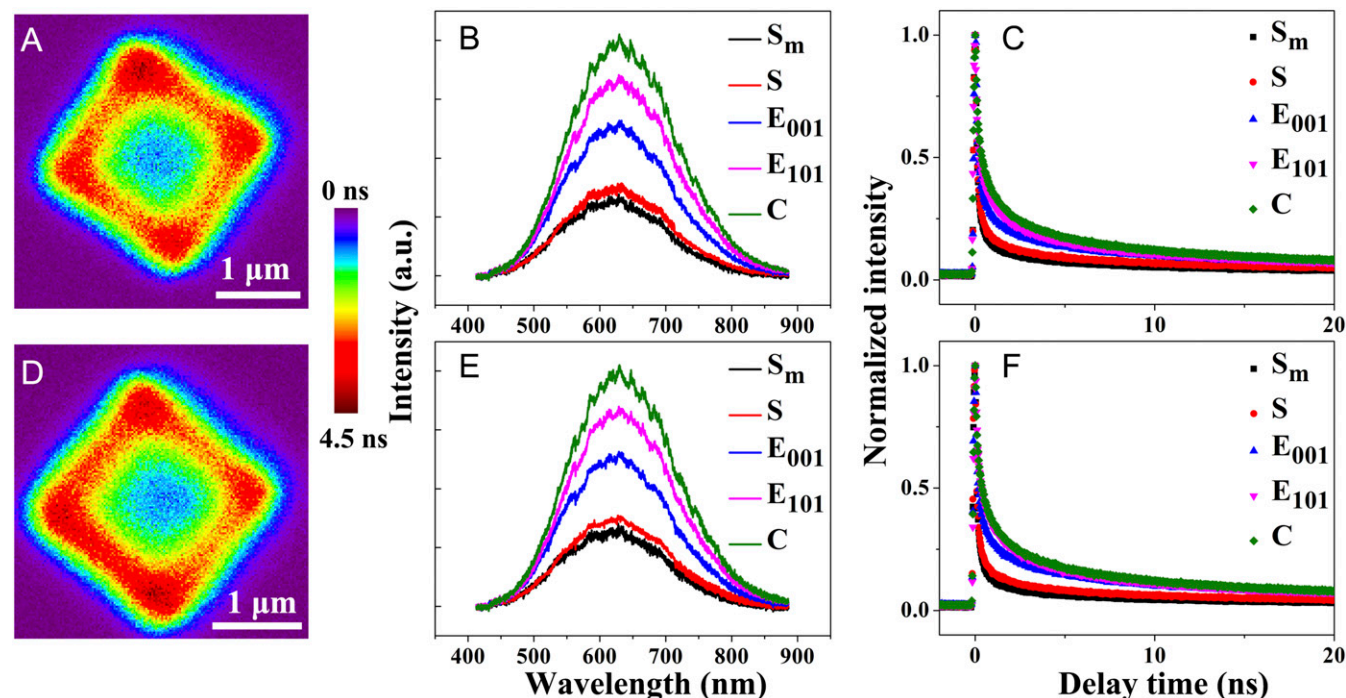

Fig. 3. (*A* and *D*) PL lifetime images of a single anatase TiO$_2$ particle (λ_{ex} = 375 nm, a femtosecond pulsed laser) (intensity bar: 0 to 4.5 ns). (*B* and *E*) The PL spectra. (*C* and *F*) The lifetime from middle site to corner site for a single anatase TiO$_2$ particle.

crystal-facet- and defect-dependent photocatalytic reductions (oxidation) of resazurin (amplex red) on individual anatase TiO₂ particles (Fig. 4). To induce the photocatalytic redox reaction and excite fluorogenic probes at the same time, simultaneous irradiations at 405 nm and 532 nm with a CW laser were respectively applied to excite a TiO₂ particle and resorufin.

Fig. 5 shows the typical quasi-TIRF images captured for anatase TiO₂ particles in a water (methanol/water) solution containing amplex red (resazurin) under 532-nm and 405-nm laser irradiations. Fig. 5A illustrates a schematic diagram for the photocatalytic oxidation reaction of amplex red on a single TiO₂ particle. A number of fluorescence bursts with signals higher than the background (*SI Appendix*, Fig. S12 *A and B*) were observed in the photoirradiation, and their locations were determined using centroid analysis. Interestingly, under all of the experimental conditions fluorescence spots were found to be preferentially located on the edges and corners of the crystal in both oxidation and reduction reactions (Fig. 5 *B–G*) (Movies S1 and S2). These results highlight the significant effects of the crystal face and defect on the photocatalytic activity, which were not observed in the bulk measurements (*SI Appendix*, Fig. S11). Similar results were obtained for the other anatase TiO₂ particles under the same conditions (*SI Appendix*, Fig. S13), ensuring the repeatability of the experiments. It is worthwhile to note that surface defects near the edges and corners served as highly active sites, which is consistent with our results on the single-particle PL lifetime mapping.

DFT Calculations of the Fluorogenic Probe Reactions on the Surfaces and Crystal Edge. To better understand the photocatalytic activity of the (001) surface, the (101) surface, and the crystal edge in a single anatase TiO₂ particle and gain further insights into the nature of different interfaces, the fluorogenic probe reaction processes were simulated on the cluster model (Fig. 6A) with DFT calculations. The density of states (DOS) of the cluster model reveals that the crystal edge exhibits other characteristics of energy band structure distinguished from the (001) surface and the (101) surface. The absolute value of the bandgap is underestimated by the density functional approach, but the relative energy level of the bands can still be used for theoretical analysis (54). The details of band alignment with the experimental bandgap are described in *SI Appendix*. As shown in Fig. 6 *B* and *C*, the conduction band minimum (CBM) and the valence band

maximum (VBM) of the crystal edge locate lower than those of the (001) surface. Thus, the photogenerated electrons (e⁻) are able to flow from the (001) surface to the edge site, while the holes (h⁺) move in the opposite direction, promoting the separation of photoexcited h⁺/e⁻ pairs. In this junction, the edge site serves as the photocatalytic reduction site for resazurin reduction. Simultaneously, both the CBM and the VBM of the (101) surface are lower than those of the crystal edge, resulting in another junction between the crystal edge and the (101) surface to allow the valence band of the edge site for photocatalytic oxidation. The results of the electronic structure indicate that the crystal edge formed by the (001) surface and the (101) surface accumulates the photogenerated electrons and holes and acts as the redox reaction site.

Furthermore, the fluorogenic probe reaction processes on the surfaces and at the crystal edge of anatase TiO₂ were calculated, and their Gibbs free energy changes (ΔG) and energy barriers (E_a) are shown in *SI Appendix*, Table S4. A previous work has shown that the photogenerated electrons and holes in the bulk of anatase TiO₂ separately migrate to the (101) facets and (001) facets and then participate in the reduction and oxidation processes in photocatalytic reactions (18). Thus, to further discover the reductive sites, the capability of resazurin reduction is compared between the crystal edge and (101) facets. The more negative ΔG value demonstrates that the crystal edge has a higher ability to enhance the equilibrium constant attributed to the accumulation of more photogenerated electrons at the crystal edge than on the (101) surface. Moreover, a similar analysis suggests that the crystal edge owing to more photogenerated holes than the (001) surface also promotes the amplex red oxidation reaction to achieve the equilibrium state. At the same time, the lower E_a of the fluorogenic probe reactions (*SI Appendix*, Table S4) further indicates that the crystal edge is a kinetically feasible site for photocatalytic reaction with a higher reaction rate. Therefore, the theoretical calculation at the atomic level demonstrates that the unique geometric configuration of the crystal edge improves the trapping probability of the photogenerated charge carriers for photocatalysis, consistent with our experimental results.

Based on the above results, the mechanism for the photogenerated electron/hole pairs transfer on a single anatase TiO₂ particle is proposed. First, due to a bandgap in the conduction band of (001) and (101) facets, more photogenerated electrons move
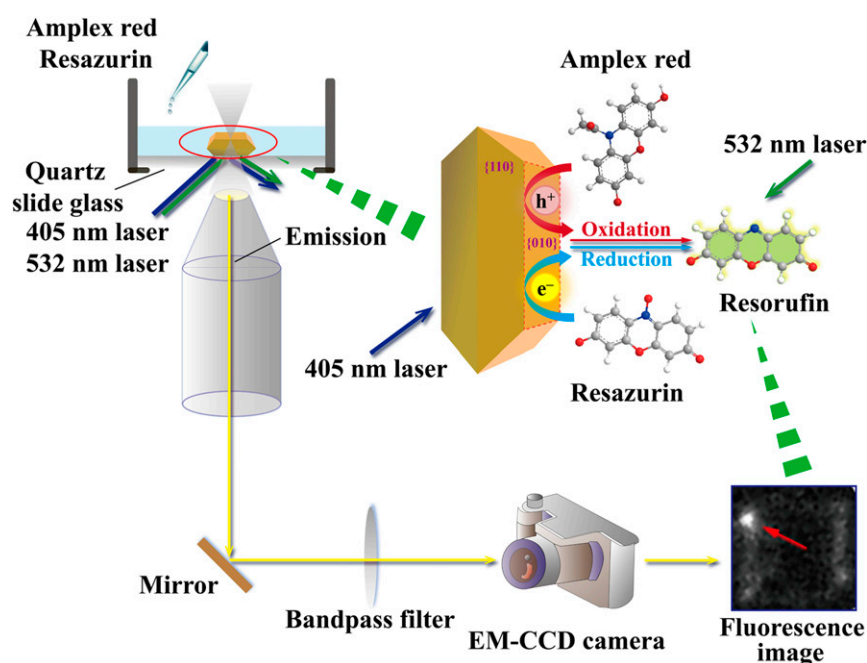

Fig. 4. A schematic diagram: single-molecule and -particle fluorescence microscopic mesurements for amplex red oxidation and resazurin reduction.

Fig. 5. A schematic diagram for the photocatalytic oxidation reaction of amplex red and the photocatalytic reduction of resazurin on a single TiO₂ particle (*A*). Single-molecule fluorescence images on a single TiO₂ particle for the photocatalytic oxidation of amplex red (*B–D*) and the photocatalytic reduction of resazurin (*E–G*) at various times. Time trace of fluorescence intensity observed over the yellow circle region (*D*, *Inset*). (Scale bar, 1 μm.)

from (001) facets to (101) facets by the surface heterojunction (edge and corner) formed by (001) facets and (101) facets. Meanwhile, more photogenerated holes can move from (101) facets to (001) facets by the surface heterojunction (edge and corner) owing to the bandgap in VB. As a result, more electrons and holes will gather near the surface heterojunction (i.e., edge and corner). Thus, on the surface heterojunction, an efficient separation of the photogenerated electron–hole pairs is achieved. Considering that the lifetime of the electron is longer and the intensity of PL is also stronger than those on other areas, the surface heterojunction (edge and corner) is the active site for oxidation/reduction.

The above observations provide convincing evidence to demonstrate the existence of the surface junction "edge or corner" on single TiO₂ particles and offer deep insights into the nature of the photocatalytic active sites. These findings also imply an activity-based strategy for rationally engineering catalysts for improved photocatalysis, which can be also applied for other catalytic materials, in addition to TiO₂. Therefore, our discovery is expected to accelerate the pace of development of next-generation photocatalysts. Furthermore, the integrated approach used in this work may offer a versatile tool in probing redox reactions in photo/electro/chemical catalysis,and heterogeneous catalytic applications.

Conclusions

In summary, we have measured the spatially and temporally resolved PL on anatase TiO₂ particles and observed the differences in charge-carrier mobility and recombination. Also, we have mapped both PL intensity and lifetime of anatase TiO₂ particles. Moreover, with the in situ single-molecule PL detection we have identified the photocatalytic oxidative/reductive sites on anatase TiO₂ particles. These results indicate that the observed PL lifetime depends on not only the bandgap between (101) and (001) facets, but also the nature and density of crystal defects. Our single-molecule and single-particle approaches provide valuable insights into the mechanism for photocatalytic reactions on TiO₂ and can be useful for reliable real-time detection of redox reactions in heterogeneous catalysis.

Experimental Methods

Chemicals and Synthesis of Anatase TiO₂ Particles. All chemicals used in this work, e.g., resazurin (Sigma-Aldrich), TiOSO₄ (Sigma-Aldrich), HF (Sigma-Aldrich), and amplex red (Thermo Fisher Scientific Inc.), were analytical-grade reagents and used without further purification. The anatase TiO₂ particles were synthesized as reported previously (the detailed experiments are described in *SI Appendix*, Text S1) (55).

Fig. 6. Cluster model of anatase TiO₂ and the electronic structures. (*A*) Model of anatase TiO₂ with both (001) and (101) surfaces and their crystal edge. The sites in the dotted boxes were used for analyzing the DOS. (*B*) DOS of the edge site, the (001) surface, and the (101) surface of the cluster model without the scissor operator. (*C*) The relatively energy level of the bands for different photocatalytic sites from the positions of the VBM and the CBM in DOS and the flow route of photogenerated charge carriers.

Characterization of Anatase TiO₂ Particles. The detailed characterization methods are described in *SI Appendix*, Text S2.

Sample Preparation for Single-Molecule Fluorescence Microscopy and Single-Particle PL Measurements. The quartz cover glasses (DAICO MFG Co.) and grid cover glasses (Matsunami Glass Inc.; thickness 0.15 to 0.18 mm) were purchased for wide-field and confocal microscopic tests, respectively. Prior to the measurements, cover glasses were thoroughly cleaned by sonication in a 20% detergent solution (As One; Cleanace) for 7 h, followed by repeated washings with warm water and Milli-Q ultrapure water (Millipore Inc.).

To obtain the isolated anatase TiO₂ particles, well-dispersed methanol suspensions at very low concentrations of TiO₂ were spin coated on a cleaned cover glass. The particle-coated cover glass was annealed at 373 K for 60 min to immobilize the particles on the glass surface. Details of the sample preparation are given in *SI Appendix*.

Single-Particle PL Measurements by Confocal Microscopy. Single-particle PL images and spectra of samples were recorded by using an objective scanning confocal microscope system (MicroTime 200; PicoQuant) coupled with an Olympus IX71 inverted fluorescence microscope. The samples were excited through an oil-immersion objective lens (UplanSApochromat; 100×, 1.4 NA Olympus) either by a circular-polarized 375-nm femtosecond pulsed laser (Spectra-Physics; Mai Tai HTS-W with an automated frequency doubler, Inspire Blue FAST-W; 0.8-MHz repetition rate) or a circular-polarized 405-nm picosecond pulsed laser controlled by a PDL-800B driver (PicoQuant). The emission from the sample was collected by the same objective and detected by a single photon avalanche photodiode (Micro Photon Devices; PDM 50CT) through a dichroic beam splitter (Chroma; 405rdc) and a long-pass filter (Chroma; HQ430CP). For the spectroscopy, only the emission that passed through a slit was detected by an EM-CCD camera (Princeton Instruments; ProEM) equipped with the imaging spectrograph (Acton Research; SP-2356). The spectra were typically integrated for 30 s. The spectrum detected by the EM-CCD camera was stored and analyzed by using a personal computer. All of the experimental data were obtained at ambient temperature.

Single-Molecule Fluorescence Measurements by Wide-Field Microscopy. The single-molecule fluorescence measurements were conducted on an Olympus IX81 inverted fluorescence microscope. The position of the anatase TiO₂ particles immobilized on the cover glass was determined from the transmission image obtained using a halogen lamp (Olympus; U-LH100L-3). Simultaneous irradiation at 405 nm and 532 nm with a CW laser (OZ Optics) was respectively used to excite a TiO₂ particle and a fluorescence probe through an oil objective

(Olympus; PlanApo 100×/1.40 oil). The emission image was collected with the same objective and recorded by an EMCCD camera (Roper Scientific; Evolve 512) through a dichroic beamsplitter (Semrock; FF552-Di02) and a band-pass filter (Semrock; FF01-575/30) to monitor the signal from a fluorescence probe selectively. The images were recorded at a frame rate of 20 frames·s⁻¹ using MetaMorph (Molecular Devices) and processed using ImageJ (National Institutes of Health) or OriginPro 8.5 (OriginLab). All experimental data were obtained at ambient temperature.

Theoretical Calculations. The fluorogenic probe reaction mechanisms on the crystal edge and the surfaces of anatase TiO₂ were explored with first-principles DFT calculations. To reflect the crystal edge, a cluster model of anatase TiO₂ with both (001) and (101) facets (see details in the model structure of *SI Appendix*, Text S3) (56) was used for simulating the electronic structure and calculating the thermodynamic and kinetic properties of fluorogenic probe reactions at different sites. All of the calculations were performed based on the plane-wave basis sets and ultrasoft pseudopotentials (57), as implemented in the CASTEP module (52). The exchange-correlation energy and potential were described self-consistently using the Perdew, Burke, and Ernzerhof (PBE) functional (58) of generalized gradient approximation (GGA). The cutoff energy and self-consistent field (SCF) tolerance were set as 340 eV and 1 × 10⁻⁴ eV/cell, respectively. The k-point mesh of the Brillouin zone sampling for this cluster model in the electronic property calculation was set at 1 × 5 × 1 based on the Monkhorst–Pack scheme, depending on the unit cell size and shape (59). The structures of the reactants and products in the reaction process on (001) facets, (101) facets, and the crystal edge of nanoscale TiO₂ were energy minimized. The transition-state structure of amplex red oxidation and resazurin reduction was searched to obtain the activation energy by linear synchronous transit (LST)/quadratic synchronous transit (QST) methods (60).

1. J. Schneider et al., Understanding TiO₂ photocatalysis: Mechanisms and materials. *Chem. Rev.* **114**, 9919–9986 (2014).
2. A. Fujishima, K. Honda, Electrochemical photolysis of water at a semiconductor electrode. *Nature* **238**, 37–38 (1972).
3. G. Liu et al., Titanium dioxide crystals with tailored facets. *Chem. Rev.* **114**, 9559–9612 (2014).
4. C. Li et al., Facet-dependent photoelectrochemical performance of TiO₂ nanostructures: An experimental and computational study. *J. Am. Chem. Soc.* **137**, 1520–1529 (2015).
5. R. Schaub et al., Oxygen-mediated diffusion of oxygen vacancies on the TiO₂(110) surface. *Science* **299**, 377–379 (2003).
6. R. Schaub et al., Oxygen vacancies as active sites for water dissociation on rutile TiO(₂)(110). *Phys. Rev. Lett.* **87**, 266104 (2001).
7. X. Q. Gong, A. Selloni, O. Dulub, P. Jacobson, U. Diebold, Small Au and Pt clusters at the anatase TiO₂(101) surface: Behavior at terraces, steps, and surface oxygen vacancies. *J. Am. Chem. Soc.* **130**, 370–381 (2008).
8. Q. Wu, R. van de Krol, Selective photoreduction of nitric oxide to nitrogen by nanostructured TiO₂ photocatalysts: Role of oxygen vacancies and iron dopant. *J. Am. Chem. Soc.* **134**, 9369–9375 (2012).
9. T. R. Gordon et al., Nonaqueous synthesis of TiO₂ nanocrystals using TiF₄ to engineer morphology, oxygen vacancy concentration, and photocatalytic activity. *J. Am. Chem. Soc.* **134**, 6751–6761 (2012).
10. J. Yu, J. Low, W. Xiao, P. Zhou, M. Jaroniec, Enhanced photocatalytic CO₂-reduction activity of anatase TiO₂ by coexposed 001 and 101 facets. *J. Am. Chem. Soc.* **136**, 8839–8842 (2014).
11. R. Li et al., Spatial separation of photogenerated electrons and holes among 010 and 110 crystal facets of BiVO4. *Nat. Commun.* **4**, 1432 (2013).
12. L. Mu, Z. Yue, A. Li, S. Wang, C. Li, Enhancing charge separation on high symmetry SrTiO₃ exposed with anisotropic facets for photocatalytic water splitting. *Energy Environ. Sci.* **9**, 2463–2469 (2016).
13. L. Mu, B. Zeng, X. Tao, Y. Zhao, C. Li, Unusual charge distribution on the facet of a SrTiO₃ nanocube under light irradiation. *J. Phys. Chem. Lett.* **10**, 1212–1216 (2019).
14. D. Li et al., Crystallographic-orientation-dependent charge separation of BiVO₄ for solar water oxidation. *ACS Energy Lett.* **4**, 825–831 (2019).
15. K. Wenderich, G. Mul, Methods, mechanism, and applications of photodeposition in photocatalysis: A review. *Chem. Rev.* **116**, 14587–14619 (2016).
16. Y. Tamaki et al., Direct observation of reactive trapped holes in TiO₂ undergoing photocatalytic oxidation of adsorbed alcohols: Evaluation of the reaction rates and yields. *J. Am. Chem. Soc.* **128**, 416–417 (2006).
17. H. Yu et al., High-performance TiO₂ photoanode with an efficient electron transport network for dye-sensitized solar cells. *J. Phys. Chem. C* **113**, 16277–16282 (2009).
18. T. Tachikawa, S. Yamashita, T. Majima, Evidence for crystal-face-dependent TiO₂ photocatalysis from single-molecule imaging and kinetic analysis. *J. Am. Chem. Soc.* **133**, 7197–7204 (2011).
19. Z. Bian, T. Tachikawa, P. Zhang, M. Fujitsuka, T. Majima, Au/TiO₂ superstructure-based plasmonic photocatalysts exhibiting efficient charge separation and unprecedented activity. *J. Am. Chem. Soc.* **136**, 458–465 (2014).
20. J. B. Sambur et al., Sub-particle reaction and photocurrent mapping to optimize catalyst-modified photoanodes. *Nature* **530**, 77–80 (2016).
21. W. Kim, T. Tachikawa, G. H. Moon, T. Majima, W. Choi, Molecular-level understanding of the photocatalytic activity difference between anatase and rutile nanoparticles. *Angew. Chem. Int. Ed. Engl.* **53**, 14036–14041 (2014).
22. D. J. Gargas et al., Engineering bright sub-10-nm upconverting nanocrystals for single-molecule imaging. *Nat. Nanotechnol.* **9**, 300–305 (2014).
23. C. Li, Z. Wang, Y. Lu, X. Liu, L. Wang, Conformation-based signal transfer and processing at the single-molecule level. *Nat. Nanotechnol.* **12**, 1071–1076 (2017).
24. J.-H. Zhong et al., Probing the electronic and catalytic properties of a bimetallic surface with 3 nm resolution. *Nat. Nanotechnol.* **12**, 132–136 (2017).
25. J. Lee, N. Tallarida, X. Chen, L. Jensen, V. A. Apkarian, Microscopy with a single-molecule scanning electrometer. *Sci. Adv.* **4**, eaat5472 (2018).
26. W. E. Moerner, New directions in single-molecule imaging and analysis. *Proc. Natl. Acad. Sci. U.S.A.* **104**, 12596–12602 (2007).
27. A. Sanamrad et al., Single-particle tracking reveals that free ribosomal subunits are not excluded from the Escherichia coli nucleoid. *Proc. Natl. Acad. Sci. U.S.A.* **111**, 11413–11418 (2014).
28. S. Tan et al., Molecular oxygen adsorption behaviors on the rutile TiO2(110)-1×1 surface: An in situ study with low-temperature scanning tunneling microscopy. *J. Am. Chem. Soc.* **133**, 2002–2009 (2011).
29. Y. Zhao et al., What are the adsorption sites for CO on the reduced TiO₂(110)-1 x 1 surface? *J. Am. Chem. Soc.* **131**, 7958–7959 (2009).
30. S. Tan et al., Observation of photocatalytic dissociation of water on terminal Ti sites of TiO2(110)-1 × 1 surface. *J. Am. Chem. Soc.* **134**, 9978–9985 (2012).

31. Y. Wang et al., Role of point defects on the reactivity of reconstructed anatase titanium dioxide (001) surface. Nat. Commun. **4**, 2214 (2013).
32. G. Haase, Surface photovoltage imaging for the study of local electronic structure at semiconductor surfaces. Int. Rev. Phys. Chem. **19**, 247–276 (2000).
33. L. Kronik, Y. Shapira, Surface photovoltage phenomena: Theory, experiment, and applications. Surf. Sci. Rep. **37**, 1–206 (1999).
34. J. Zhao, F. E. Osterloh, Photochemical charge separation in nanocrystal photocatalyst films: Insights from surface photovoltage spectroscopy. J. Phys. Chem. Lett. **5**, 782–786 (2014).
35. J. Wang, J. Zhao, F. E. Osterloh, Photochemical charge transfer observed in nanoscale hydrogen evolving photocatalysts using surface photovoltage spectroscopy. Energy Environ. Sci. **8**, 2970–2976 (2015).
36. J. Zhu et al., Direct imaging of highly anisotropic photogenerated charge separations on different facets of a single $BiVO_4$ photocatalyst. Angew. Chem. Int. Ed. Engl. **54**, 9111–9114 (2015).
37. J. Park et al., Single-molecule recognition of biomolecular interaction via Kelvin probe force microscopy. ACS Nano **5**, 6981–6990 (2011).
38. R. Chen, F. Fan, T. Dittrich, C. Li, Imaging photogenerated charge carriers on surfaces and interfaces of photocatalysts with surface photovoltage microscopy. Chem. Soc. Rev. **47**, 8238–8262 (2018).
39. Y. Gao et al., Directly probing charge separation at interface of TiO_2 phase junction. J. Phys. Chem. Lett. **8**, 1419–1423 (2017).
40. R. Chen et al., Charge separation via asymmetric illumination in photocatalytic Cu_2O particles. Nat. Energy **3**, 655–663 (2018).
41. Y. Zhu, P. A. Salvador, G. S. Rohrer, Buried charge at the $TiO_2/SrTiO_3$ (111) interface and its effect on photochemical reactivity. ACS Appl. Mater. Interfaces **9**, 7843–7851 (2017).
42. A. S. Pisat et al., Spatial selectivity of photodeposition reactions on polar surfaces of centrosymmetric ferroelastic γ-WO_3. J. Mater. Chem. A **5**, 8261–8266 (2017).
43. J. J. Glickstein, P. A. Salvador, G. S. Rohrer, Multidomain simulations of coated ferroelectrics exhibiting spatially selective photocatalytic activity with high internal quantum efficiencies. J. Mater. Chem. A **4**, 16085–16093 (2016).
44. S. A. Claridge, J. J. Schwartz, P. S. Weiss, Electrons, photons, and force: Quantitative single-molecule measurements from physics to biology. ACS Nano **5**, 693–729 (2011).
45. N. Zou et al., Imaging catalytic hotspots on single plasmonic nanostructures via correlated super-resolution and electron microscopy. ACS Nano **12**, 5570–5579 (2018).
46. N. Zou et al., Cooperative communication within and between single nanocatalysts. Nat. Chem. **10**, 607–614 (2018).
47. M. Hesari, X. Mao, P. Chen, Charge carrier activity on single-particle photo(electro) catalysts: Toward function in solar energy conversion. J. Am. Chem. Soc. **140**, 6729–6740 (2018).
48. Z. Zheng, T. Tachikawa, T. Majima, Single-particle study of Pt-modified Au nanorods for plasmon-enhanced hydrogen generation in visible to near-infrared region. J. Am. Chem. Soc. **136**, 6870–6873 (2014).
49. Z. Zheng, T. Tachikawa, T. Majima, Plasmon-enhanced formic acid dehydrogenation using anisotropic Pd-Au nanorods studied at the single-particle level. J. Am. Chem. Soc. **137**, 948–957 (2015).
50. J. Guan et al., Direct single-molecule dynamic detection of chemical reactions. Sci. Adv. **4**, eaar2177 (2018).
51. A. Agrawal, R. Deo, G. D. Wang, M. D. Wang, S. Nie, Nanometer-scale mapping and single-molecule detection with color-coded nanoparticle probes. Proc. Natl. Acad. Sci. U.S.A. **105**, 3298–3303 (2008).
52. M. D. Segall et al., First-principles simulation: Ideas, illustrations and the CASTEP code. J. Phys. Condens. Matter **14**, 2717–2744 (2002).
53. C. Bueno et al., The excited-state interaction of resazurin and resorufin with amines in aqueous solutions. Photophysics and photochemical reactions. Photochem. Photobiol. **76**, 385–390 (2002).
54. F. De Angelis, C. Di Valentin, S. Fantacci, A. Vittadini, A. Selloni, Theoretical studies on anatase and less common TiO_2 phases: Bulk, surfaces, and nanomaterials. Chem. Rev. **114**, 9708–9753 (2014).
55. J. Pan, G. Liu, G. Q. Lu, H. M. Cheng, On the true photoreactivity order of 001, 010, and 101 facets of anatase TiO2 crystals. Angew. Chem. Int. Ed. Engl. **50**, 2133–2137 (2011).
56. A. Y. Zhang, W. Wang, J. J. Chen, C. Liu, H. Q. Yu, Epitaxial facet junction on TiO_2 single crystals for efficient photocatalytic water splitting. Energy Environ. Sci. **11**, 1444–1448 (2018).
57. D. Vanderbilt, Soft self-consistent pseudopotentials in a generalized eigenvalue formalism. Phys. Rev. B Condens. Matter **41**, 7892–7895 (1990).
58. J. P. Perdew, K. Burke, M. Ernzerhof, Generalized gradient approximation made simple. Phys. Rev. Lett. **77**, 3865–3868 (1996).
59. H. J. Monkhorst, J. D. Pack, Special points for brillouin-zone integrations. Phys. Rev. B **13**, 5188–5192 (1976).
60. T. A. Halgren, W. N. Lipscomb, The synchronous-transit method for determining reaction pathways and locating molecular transition states. Chem. Phys. Lett. **49**, 225–232 (1977).

CHEMISTRY